

Supplemental Material: Atomic-Ordering-Induced Quantum Phase Transition between Topological Crystalline Insulator and Z_2 Topological Insulator

Hui-Xiong Deng(邓惠雄)^{1,2,*} Zhi-Gang Song(宋志刚)¹ Shu-Shen Li(李树深)^{1,2,3} Su-Huai Wei(魏苏淮)^{4,†} and Jun-Wei Luo(骆军委)^{1,2,3,‡}

¹State Key Laboratory of Superlattices and Microstructures, Institute of Semiconductors, Chinese Academy of Sciences, P. O. Box 912, Beijing 100083, China

²University of Chinese Academy of Sciences, Beijing 100049, China

³Beijing Academy of Quantum Information Sciences, Beijing 100193, China

⁴Beijing Computational Science Research Center, Beijing 100094, China

I. BAND-EDGE EVOLUTIONS OF SnTe AND PbTe AS A FUNCTION OF UNIAXIAL STRAIN ALONG [111] DIRECTION.

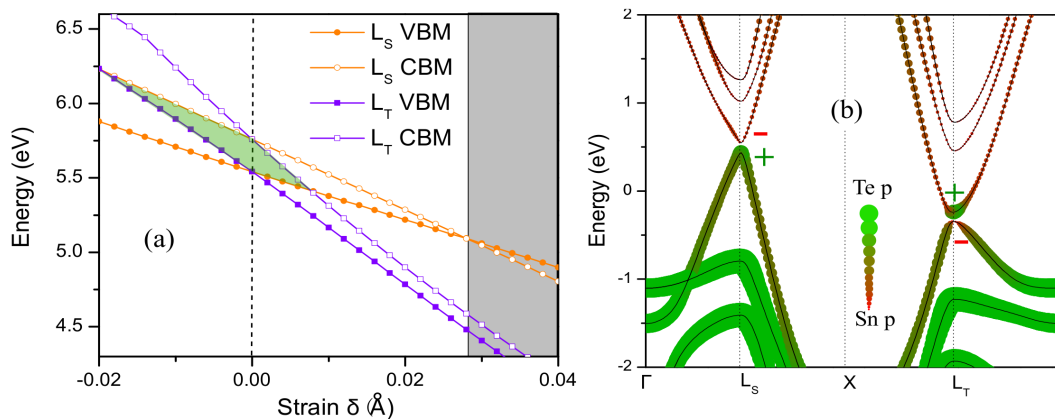


FIG. 1. (Color online) The evolutions of band-edges as function of [111] uniaxial strain. **a.** The band-edge evolutions of SnTe at the L (0.5,0.5,0.5) valley (labeled as L_S) and remaining three equivalent L valleys (labeled as L_T) as a function of uniaxial strain δ along [111] direction. In the green shadow area the SnTe is a insulator with a gap, and in the gray shadow area there is a odd number of band inversion (i.e., L_S point is back to normal band order, and the L_T point is still inverted). **b.** Band structure of SnTe with the application of the [111]-oriented uniaxial strain $\delta=0.042$. The wide green and narrow red lines indicate the band is dominated the Te p and Sn p states, respectively, and corresponding parities are also labeled.

Fu et al.[1] proposed in their pioneering study of Z_2 TIs that an uniaxial strain along the [111] direction could lift the equivalence of four L points in the $\text{Pb}_{1-x}\text{Sn}_x\text{Te}$ alloy, leading to the bandgap at the L point along the [111] direction (labeled as L_S) different from that of remaining three equivalent L points (labeled as L_T). They therefore postulated that the strained $\text{Pb}_{1-x}\text{Sn}_x\text{Te}$ alloy might have odd number of band inversion at certain composition and become a Z_2 TI. Here, we have assessed this idea in detail in terms of examining the band-edge evolutions of the end constitute SnTe as a function of uniaxial strain along the [111] direction by performing first-principles calculations. Fig. 1 shows that the equivalence of four L points in the rocksalt structure is indeed broken and band-edges at the

* hxdeng@semi.ac.cn

† suhuaiwei@csrc.ac.cn

‡ jwluo@semi.ac.cn

L_S point shift away from that of remaining three equivalent L_T points once an uniaxial strain is applied along the [111] direction with their energy deviations being proportional to strain strength δ . However, it is almost impossible to find a case having simultaneously a global bandgap and odd times of band inversions. We find that the bandgap deformation at the L_S point is much larger than that at the L_T point, which enables us to drive bandgap at the L_S back to normal order leaving behind bandgap at remaining three L_T points keeping inverted. But, deformation potentials of both conduction band valence band-edges at the L_T point are so negative that before driving L_S -valley band gap back to normal order the uniaxial strain already moves the L_T bandgap fully out the L_S bandgap leading to vanishing of global bandgap and SnTe become metallic, as shown in Fig.1(b). The gray shadow area in Fig.1(a) indicates the global bandgap of strained SnTe. Although we archive the odd number of band inversion after the transition of the bandgap order at the L_S point to normal, the transition point is too way from the shadow area, leading to the conduction band edge at the L_T valley is lower in energy than the valence band edge at the L_S point and strained SnTe becomes a metallic, as shown in the Fig. 1(b) for the band structure of SnTe with $\delta=0.042$. We have verified that this fact is also true for PbTe that when odd number of band inversions occurs, it is no longer a insulator.

II. IDENTIFY THE GROUND CRYSTAL STRUCTURE OF ROCKSALT $A_xB_{1-x}C$ ALLOYS.

To determine the ground crystal structure of rocksalt $A_xB_{1-x}C$ (A or B=Ge, Sn, Pb, C=Te, Se) alloys, we have calculated the alloy formation energies $\Delta H_f(\sigma, A_xB_{1-x}C)$ at composition $x = 0.5$ for most commonly observed alloy configurations σ [2], which include ordered CuPt, CuAu, chalcopyrite, Y2, and Z2 structures as well as a random alloy described using the ‘‘special quasi random structures’’ (SQS) approach[3]. The predicted results using first-principles calculations are summarized in Table S1. We found unambiguously that in all investigated systems, the CuPt ordered configuration has the lowest formation energy among all examined configurations, owing to CuPt-ordered structure allows all nearest cation-anion bond lengths to attain their respective equilibrium lattice with the minimum bond bending and holds the smallest strain energy among all studied configurations [2].

TABLE I. Calculated formation energies (unit in meV/4-atom) of rocksalt $A_xB_{1-x}C$ (A or B=Ge, Sn, Pb, C=Te, Se) alloys at composition $x = 0.5$ with varying configurations of ordered CuPt, CuAu, chalcopyrite, Y2, and Z2 structures as well as a SQS random alloy structure.

systems	CuPt	CuAu	Y2	Z2	CH	SQS
$\text{Sn}_{0.5}\text{Pb}_{0.5}\text{Te}$	11	21	15	17	17	12
$\text{Sn}_{0.5}\text{Pb}_{0.5}\text{Se}$	11	19	15	15	14	13
$\text{Ge}_{0.5}\text{Sn}_{0.5}\text{Te}$	18	116	49	81	75	45
$\text{Ge}_{0.5}\text{Sn}_{0.5}\text{Se}$	40	157	74	106	102	69
$\text{Ge}_{0.5}\text{Pb}_{0.5}\text{Te}$	58	256	111	169	170	100
$\text{Ge}_{0.5}\text{Pb}_{0.5}\text{Se}$	98	329	153	217	218	137
$\text{GeSe}_{0.5}\text{Te}_{0.5}$	19	129	54	80	85	52
$\text{SnSe}_{0.5}\text{Te}_{0.5}$	20	142	60	85	93	49
$\text{PbSe}_{0.5}\text{Te}_{0.5}$	23	145	78	94	93	54

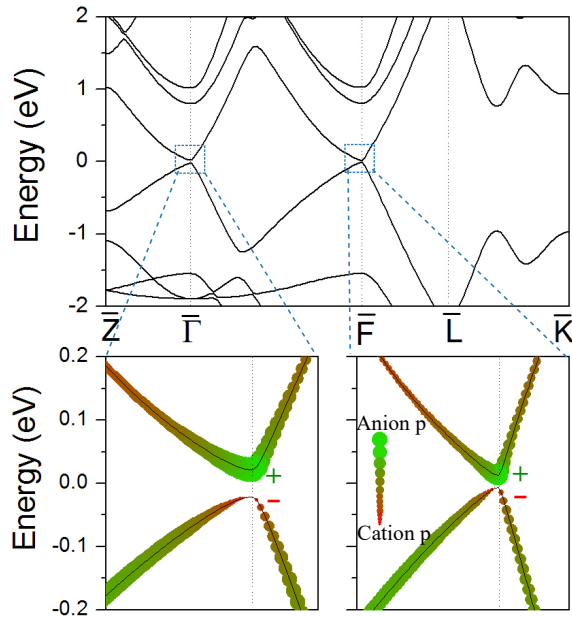


FIG. 2. (Color online) Band structure of CuPt-ordered PbSnTe₂ alloy under the equilibrium lattice constant. The wide green and narrow red lines indicate the band dominated by the anion (Te) p and cation (Sn and Pb) p orbitals, respectively. The parity symmetry is also labeled.

III. BAND STRUCTURE OF CuPt-ORDERED PbSnTe₂ ALLOY UNDER THE EQUILIBRIUM LATTICE CONSTANT.

Figure 2 shows the band structure of CuPt-ordered PbSnTe₂ alloy under the equilibrium lattice constant. Along with the transform of equivalent four L points in parent PbTe and SnTe to one $\bar{\Gamma}$ and three \bar{F} points in CuPt-ordered PbSnTe₂ alloy, energy gaps at the $\bar{\Gamma}$ and \bar{F} points are now different remarkably, which is caused by inter-band coupling as a result of symmetry reduction from (rocksalt) O_h to (CuPt-type structure) D_{3d} . After analyzing the characters of band-edge wave functions, we found that the conduction band edges at both $\bar{\Gamma}$ and \bar{F} points, mainly comes from the anion p orbit with an even parity (“+”), and the valence band edges from the cation p orbit with an odd parity (“-”), illustrating the bandgaps at both $\bar{\Gamma}$ and \bar{F} points being inverted and hence the PbSnTe₂ alloy being a TCI under equilibrium condition.

IV. CALCULATIONS OF TOPOLOGICAL INVARIANT Z_2 .

The Z_2 index in 2D systems is a single invariant, but in 3D system is a complex of four invariants, i.e., $Z_2=(\nu_0; \nu_1\nu_2\nu_3)$, where ν_0 is the strong topological index and ν_1, ν_2 , and ν_3 are three weak indices ($\nu_0 = 1$ alone indicates a strong topological insulator without inquiring $\nu_1\nu_2\nu_3$; $\nu_0 = 0$ is a weak topological insulator if at least one of ν_1, ν_2, ν_3 equal to 1). Only the strong topological insulator ($\nu_0=1$), which is named as a Z_2 TI, has robust topological surface states protected by time-reversal symmetry and against weak disorders. According to the time-reversal polarization theory developed by Fu and Kane[4], the integer Z_2 invariant of a time-reversal (\mathcal{T}) symmetric system can be written as $\Delta = P_\theta(T/2) - P_\theta(0) \text{ mod } 2$, where P_θ is defined as the “time-reversal polarization”. Later, Soluyanov and Vanderbilt [5] further simplified this method by utilizing Wannier functions as a basis set, and implemented it within the *ab initio* plan-wave calculations. They suggested that we can simply calculate the Z_2 invariant by tracking the spectrum of Wannier charge centers (WCCs) $\bar{\chi}_n$ and determining the center of the largest gap z^m between two adjacent WCCs

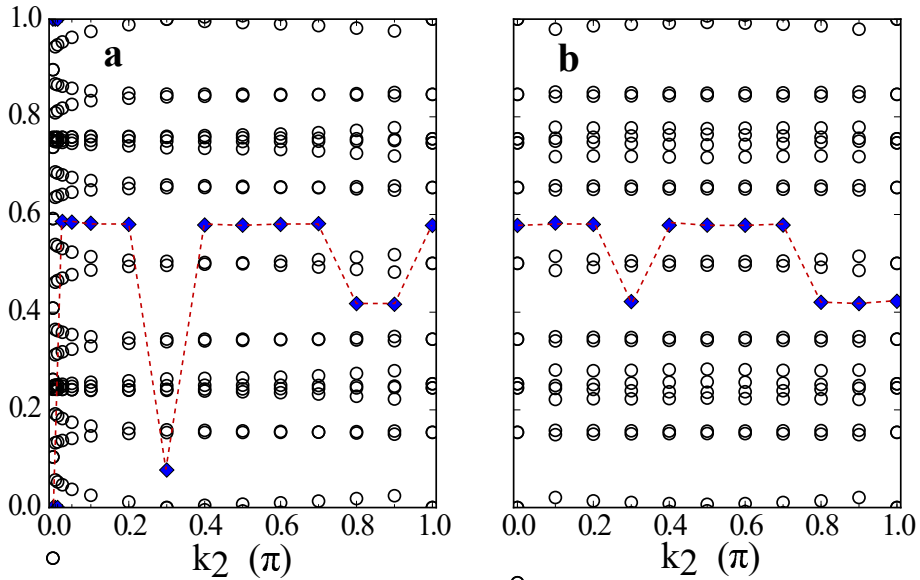


FIG. 3. (Color online) Evolution of WCCs $\bar{\chi}_n$ of CuPt ordered $\text{Sn}_{0.5}\text{Pb}_{0.5}\text{Te}$ alloy in the r_3 direction vs k_2 at (a) $n_1=0$; (b) $n_1=1$. Blue rhombus indicates the midpoint of largest gap. k_2 is sampled in 14 increments from 0 to π . From this figure, it is seen that for the $n_1=0$ surface it has a odd number of jumps of the $\bar{\chi}_n$, so the $\nu_0 = 1$, and for $n_1=1$ surface has a even number of jumps of the $\bar{\chi}_n$, so the $\nu_1 = 0$. Furthermore, the $R\bar{3}m$ symmetry in the CuPt structure guarantees the $\nu_1=\nu_2=\nu_3=0$. Thus, the $Z_2 = (1:000)$.

on the circle. The overall Z_2 invariant can then be obtained as,

$$\Delta = \sum_{m=0} \Delta_m \text{ mod } 2 \quad . \quad (1)$$

$$(-1)^{\Delta_m} = \prod_{n=1}^{\mathcal{N}} \text{sgn}[g(2\pi z^m, 2\pi z^{m+1}, 2\pi \bar{\chi}_n^{m+1})]$$

where $\text{sgn}(x)$ is the sign function, and $g(\phi_1, \phi_2, \phi_3) = \sin(\phi_2 - \phi_1) + \sin(\phi_3 - \phi_2) + \sin(\phi_1 - \phi_3)$, which is the directed area of a triangle defined by angles ϕ_1, ϕ_2, ϕ_3 on a unit circle. \mathcal{N} is the number of occupied bands. For more details about these method, please refer to the Fu and Soluyanov's papers[4, 5].

Due to the CuPt-ordered $\text{Sn}_{0.5}\text{Pb}_{0.5}\text{Te}$ alloy has a $R\bar{3}m$ symmetry, which has a threefold rotational axis leading to $\nu_1=\nu_2=\nu_3$, one only needs to calculate one weak Z_2 index ν_1 , i.e. $n_1=1$ surface of the parallelepiped constructed by the eight time-reversal points in the reciprocal space. Similarly, one only needs to calculate one more of the Z_2 invariants for $n_1=0$ surface to get the strong topological index ν_0 . Figure 3 shows the calculated evolution of WCCs $\bar{\chi}_n$ of CuPt-ordered $\text{Sn}_{0.5}\text{Pb}_{0.5}\text{Te}$ alloy upon application of 1.13% tensile strain in the r_3 direction vs k_2 at (a) $n_1=0$ (i.e. $k_1=0$); (b) $n_1=1$ (i.e. $k_1=\pi$). We found that for the $n_1=0$ surface, the gap center jumps over 11 WCCs near the $k_2=0$, and over 10 WCCs at $k_2=0.2$ and $k_2=0.3$, and then over 2 WCCs at $k_2=0.7$ and $k_2=0.9$, respectively. Thus, the total number of jumps is $11+10+10+2+2=35$, an odd number. For the $n_1=1$ surface, similarly, we get a total of $2+2+2=6$ jumps, which is even number. In terms of the Eq. (1), we obtain $\nu_0 = 1$, and $\nu_1 = \nu_2 = \nu_3 = 0$ ($Z_2 = (1:000)$), and hence CuPt-ordered $\text{Sn}_{0.5}\text{Pb}_{0.5}\text{Te}$ alloy upon application of 1.13% tensile strain is a strong Z_2 TI.

V. EFFECTIVE HAMILTONIAN MODEL FOR CALCULATING TOPOLOGICAL SURFACE STATES AT Z_2 TI PHASE.

We can use the model Hamiltonian method to simulate semi-infinite slabs. Most of Z_2 TIs such as Bi_2Se_3 , Bi_2Te_3 , Sb_2Te_3 as well as $\text{Sn}_{0.5}\text{Pb}_{0.5}\text{Te}$ alloy in Z_2 phase the band inversions occur at the Γ point, we are able to calculate the topological surface band structure using a simple low-energy effective Hamiltonian $H_\Gamma(k)$ near the Γ point [6]. The symmetry of Γ point in CuPt-ordered $\text{Sn}_{0.5}\text{Pb}_{0.5}\text{Te}$ alloy belongs to the space group D_{3d} which is same as in Bi_2Se_3 , the low-energy effective Hamiltonian $H_\Gamma(k)$ near Γ point for CuPt-ordered PbSnTe_2 alloy is therefore written as [6],

$$H_\Gamma(\mathbf{k}) = \epsilon_0(\mathbf{k}) \mathbf{I}_{4 \times 4} + \begin{pmatrix} M(\mathbf{k}) & A_1 k_z & 0 & A_2 k_- \\ A_1 k_z & -M(\mathbf{k}) & A_2 k_- & 0 \\ 0 & A_2 k_+ & M(\mathbf{k}) & -A_1 k_z \\ A_2 k_+ & 0 & -A_1 k_z & -M(\mathbf{k}) \end{pmatrix} \quad (2)$$

where $k_\parallel^2 = k_x^2 + k_y^2$, $k_\pm = k_x \pm ik_y$. $\epsilon_0(k) = C + D_1 k_z^2 + D_2 k_\parallel^2$ and $M(k) = m - B_1 k_z^2 - B_2 k_\parallel^2$. All of these parameters in the effective model can be obtained by fitting the energy spectrum of the effective Hamiltonian with that of the first-principles calculations.

In order to explore surface states of the semi-infinite slabs, we calculate the surface Green Function (GF) according to Refs.[7, 8]. Here a simple description about the process is shown. The equation of Green Function of the semi-infinite slabs is following:

$$\begin{pmatrix} \epsilon - H_s & H_{SR} \\ H_{SR}^\dagger & \epsilon - H_R \end{pmatrix} \begin{pmatrix} G_s & G_{SR} \\ G_{RS} & G_R \end{pmatrix} = \mathbf{I} \quad (3)$$

where H_S is a $N \times N$ matrix which represents the hamiltonian of surface and H_R is a $\infty \times \infty$ matrix which represents the bulk. Both of them can be constructed through the effective hamiltonian by introducing $k_i \rightarrow \frac{1}{R_i} \sin(k_i R_i)$ and $k_i^2 \rightarrow \frac{2}{R_i^2} [1 - \cos(k_i R_i)]$. The Eq.(3) can be written in another format:

$$\begin{cases} G_s = (\epsilon - H_s - \Sigma_R)^{-1} \\ \Sigma_R = H_{SR} g_R H_{SR}^\dagger \\ g_R = (\epsilon - H_R)^{-1} \end{cases} \quad (4)$$

where Σ_R denotes the self-energy induced by H_R and G_S denotes the surface green function. As the H_R is a $\infty \times \infty$ matrix, which cannot be directly solved, we utilize the iteration numerical method to solve above equation. Dividing the H_R into two parts $H_R \rightarrow H_{R_0} + H_{R'}$, we can write similar equations as Eq.(3):

$$\begin{pmatrix} \epsilon - H_{R_0} & H_{R_0 R'} \\ H_{R_0 R'}^\dagger & \epsilon - H_{R'} \end{pmatrix} \begin{pmatrix} g_{R_0} & g_{R_0 R'} \\ g_{R' R_0} & g_{R'} \end{pmatrix} = \mathbf{I} \quad (5)$$

In addition, the nearest layer hopping along the slab direction will add some limitation:

$$H_{SR} = \begin{pmatrix} H_{SR_0} \\ H_{SR'} \end{pmatrix} \approx \begin{pmatrix} H_{SR_0} \\ 0 \end{pmatrix} \quad (6)$$

Thus, the self-energy part can be given as:

$$\Sigma_R = H_{SR} g_R H_{SR}^\dagger = \begin{pmatrix} H_{SR_0} & 0 \end{pmatrix} \begin{pmatrix} g_{R_0} & g_{R_0 R'} \\ g_{R' R_0} & g_{R'} \end{pmatrix} \begin{pmatrix} H_{SR_0} \\ 0 \end{pmatrix} = H_{SR_0} g_{R_0} H_{SR_0}^\dagger \quad (7)$$

Now, having transformed an $\infty \times \infty$ problem into a $N \times N$ problem, we need to obtain the g_{R_0} . The g_R green function is

$$\begin{pmatrix} \epsilon - H_{R_0} & -H_{R_0, R_1} & 0 & \cdots \\ -H_{R_0, R_1}^\dagger & \epsilon - H_{R_0} & -H_{R_0, R_1} & \cdots \\ 0 & -H_{R_0, R_1}^\dagger & \epsilon - H_{R_0} & \cdots \\ \vdots & \vdots & \vdots & \ddots \end{pmatrix} \begin{pmatrix} g_{R_0} & g_{R_0, R_1} & g_{R_0, R_2} & \cdots \\ g_{R_1, R_0} & g_{R_0} & g_{R_1, R_2} & \cdots \\ g_{R_2, R_0} & g_{R_2, R_1} & g_{R_0} & \cdots \\ \vdots & \vdots & \vdots & \ddots \end{pmatrix} = \mathbf{I} \quad (8)$$

We can write above as the linear format:

$$\begin{cases} (\epsilon - H_{R_0}) g_{R_0} = \mathbf{I} + H_{R_0, R_1} g_{R_1, R_0} \\ (\epsilon - H_{R_0}) g_{R_1, R_0} = H_{R_0, R_1}^\dagger g_{R_0} + H_{R_0, R_1} g_{R_2, R_0} \\ \vdots \\ (\epsilon - H_{R_0}) g_{R_n, R_0} = H_{R_0, R_1}^\dagger g_{R_{n-1}, R_0} + H_{R_0, R_1} g_{R_{n+1}, R_0} \end{cases} \quad (9)$$

By defining

$$\begin{cases} t_0 = (\epsilon - H_{R_0})^{-1} H_{R_0, R_1}^\dagger \\ \tilde{t}_0 = (\epsilon - H_{R_0})^{-1} H_{R_0, R_1} \\ t_i = (\mathbf{I} - t_{i-1} \tilde{t}_{i-1} - \tilde{t}_{i-1} t_{i-1})^{-1} t_{i-1}^2 \\ \tilde{t}_i = (\mathbf{I} - t_{i-1} \tilde{t}_{i-1} - \tilde{t}_{i-1} t_{i-1})^{-1} \tilde{t}_{i-1}^2 \end{cases} \quad (10)$$

Eq.(9) can be transformed into

$$\begin{cases} g_{R_1, R_0} = t_0 g_{R_0} + \tilde{t}_0 g_{R_2, R_0} \\ g_{R_2, R_0} = t_1 g_{R_0} + \tilde{t}_1 g_{R_2, R_0} \\ \vdots \\ g_{R_{2n}, R_0} = t_n g_{R_0} + \tilde{t}_n g_{R_{2n+1}, R_0} \\ \vdots \end{cases} \quad (11)$$

When $n \rightarrow \infty$, $t_n \tilde{t}_n$ will tend to 0 and the g_{R_{2n}, R_0} also will tend to 0. we need to do a truncation.

$$\begin{aligned} g_{R_1, R_0} &= t_0 g_{R_0} + \tilde{t}_0 g_{R_2, R_0} \\ &= t_0 g_{R_0} + \tilde{t}_0 t_1 g_{R_0} + \tilde{t}_1 g_{R_2, R_0} \\ &\quad \dots \\ &= (t_0 + \tilde{t}_0 t_1 + \tilde{t}_0 \tilde{t}_1 t_2 + \cdots + \tilde{t}_0 \tilde{t}_1 \cdots t_N) g_{R_0} + \tilde{t}_1 \tilde{t}_2 \cdots \tilde{t}_N g_{R_{2N}, R_0} \\ &\approx T g_{R_0} \end{aligned}$$

where

$$T = (t_0 + \tilde{t}_0 t_1 + \tilde{t}_0 \tilde{t}_1 t_2 + \cdots + \tilde{t}_0 \tilde{t}_1 \cdots t_N) \quad (12)$$

Take above into Eq.(9) we can get

$$g_{R_0} = (\epsilon - H_{R_0} - H_{R_0, R_1} T)^{-1} \quad (13)$$

Finally, we obtain the semi-infinite system green function

$$\begin{cases} G_s = (\epsilon - H_s - \Sigma_R)^{-1} \\ \Sigma_R = H_{SR_0} g_{R_0} H_{SR_0}^\dagger \\ g_{R_0} = (\epsilon - H_{R_0} - H_{R_0, R_1} T)^{-1} \end{cases} \quad (14)$$

Therefore, the local densities of states can be obtained:

$$N(\mathbf{k}_{||}, \epsilon + i\eta) = -\frac{1}{\pi} \text{Im} \sum_{\alpha} G_s^{\alpha, \alpha}(\mathbf{k}_{||}, \epsilon + i\eta) \quad (15)$$

Based on above method, we have calculated the topological surface structure of CuPt-ordered $\text{Sn}_{0.5}\text{Pb}_{0.5}\text{Te}$ alloy in Z_2 phase, as shown in Fig. 3h in main text.

VI. DETAILS OF FIRST-PRINCIPLES COMPUTATIONAL METHOD.

To engineer the band structure of alloys, we perform the first-principles calculations using the frozen-core projector-augmented wave method (PAW) within the density functional theory (DFT)[9, 10] and generalized-gradient-approximation (GGA) to the exchange-correlation potential as implemented in the VASP code[11–13]. We have carefully examined the convergence of the plane-wave cutoff energy and the Monkhorst-Pack k-point mesh. In all calculations, all the atoms are allowed to relax until the quantum mechanical forces acting on them become less than 0.02 eV/Å. The spin-orbit coupling (SOC) term is included. Regarding semi-local exchange-correlation functionals, such as GGA, usually remarkably underestimate the bandgaps of semiconductors[14], as a comparison, we have also employed the modified Becke and Johnson exchange potential (hereafter called TB-MBJ), which has the comparable accuracy with the hybrid functional and GW method, but much less computational cost[15]. For example, the TB-MBJ calculated normal gap of PbTe and inverted gap of SnTe are 0.20 eV and -0.19 eV, respectively, very close to experimental values. The random alloys are mimicked by the special quasirandom structures (SQS)[3, 16].

Different from model Hamiltonian method to calculate the topological surface band structure, in the atomistic first-principles approach we are free from the need to judge at the outset which selected 3D bulk bands will couple in surface. We do so by solving the surface band structure using explicitly the microscopic potential of a slab constructed by SnPbTe_2 alloy along the (001) direction, in which the slab nanostructure is viewed as a system in its own right rather than express it in terms of a preselected basis drawn from its bulk parent bands. The slab having e.g., 21 atomic layers, is sandwiched between 20 Å thick vacuum layers along the (001) direction. Since one slab has unavoidable two pristine surfaces (i.e., top and bottom surfaces), there always exist two Dirac cones: one on the top surface and another on the bottom surface. The symmetry of the 2D slabs enforces these two Dirac cones coupling each other, opening a topological Dirac gap. Attempt to reduce this coupling effect by splitting two Dirac cones in energy, we use the pseudo-Hydrogen (PH) to passivate the dangling bonds on top surface and leave behind the dangling bonds on the bottom surface unpassivated. However, at Z_2 TI phase, we still observe a finite Dirac gap, which is almost vanished at TCI phase. As shown in Fig. 3 in the main text, the magnitude of the Dirac gap drops remarkably as expected, owing to reduced coupling between two surface Dirac cones as increasing the slab thickness. Such surface bandgap is an intrinsic feature of finite slabs and films, and is frequently observed in thin films of prototype 3D chalcogenide TIs.

[1] Fu L and Kane C L 2007 Phys. Rev. B **76** 045302

[2] Wei S H and Zunger A 1997 Phys. Rev. B **55** 13605

- [3] Zunger A, Wei S H, Ferreira L G and Bernard J E 1990 Phys. Rev. Lett. **65** 353
- [4] Fu L and Kane C L 2006 Phys. Rev. B **74** 195312
- [5] Soluyanov A A and Vanderbilt D 2011 Phys. Rev. B **83** 235401
- [6] Zhang H, Liu C X, Qi X L, Dai X, Fang Z and Zhang S C 2009 Nat. Phys. **5** 438
- [7] Sancho M P L, Sancho J M L and Rubio J 1984 Journal of Physics F: Metal Physics **14** 1205
- [8] Sancho M P L, Sancho J M L and Rubio J 1985 Journal of Physics F: Metal Physics **15** 851
- [9] Kohn W and Sham L J 1965 Phys. Rev. **140** A1133
- [10] Hohenberg P and Kohn W 1964 Phys. Rev. **136** B864
- [11] Kresse G and Hafner J 1993 Phys. Rev. B **47** 558
- [12] Kresse G and Hafner J 1993 Phys. Rev. B **48** 13115
- [13] Kresse G and Furthmuller J 1996 Comput. Mater. Sci. **6** 15
- [14] Perdew J P and Levy M 1983 Phys. Rev. Lett. **51** 1884
- [15] Tran F and Blaha P 2009 Phys. Rev. Lett. **102** 226401
- [16] Wei S H, Ferreira L G, Bernard J E and Zunger A 1990 Phys. Rev. B **42** 9622